

Aerosol optical properties in the marine boundary layer during the First Aerosol Characterization Experiment (ACE 1) and the underlying chemical and physical aerosol properties

P. K. Quinn, D. J. Coffman, V. N. Kapustin, and T. S. Bates

Pacific Marine Environmental Laboratory, NOAA, Seattle, Washington
Joint Institute for the Study of the Atmosphere and Ocean, University of Washington, Seattle

D. S. Covert

Department of Atmospheric Sciences, University of Washington, Seattle
Joint Institute for the Study of the Atmosphere and Ocean, University of Washington, Seattle

Abstract. Measurements were made onboard the NOAA R/V *Discoverer* during the First Aerosol Characterization Experiment (ACE 1) to understand the optical properties of a minimally perturbed natural aerosol system in terms of its chemical and physical properties. ACE 1 took place during November and December of 1995 in the Southern Ocean region south of Australia. Reported here are observations at a wavelength of 550 nm of the submicron and supermicron aerosol scattering coefficient, σ_{sp} ; single scattering albedo, ω_o ; and the hemispheric backscattered fraction and mass scattering efficiencies of non-sea-salt sulfate, sea salt, and the total aerosol. Also presented is the Ångström exponent, α , for the 450 and 700 nm wavelength pair. Variations in these parameters were found to be a strong function of the relative concentrations and size distributions of the dominant aerosol chemical components. Both the submicron and supermicron aerosol mass were composed primarily of water-soluble ionic species. This is in agreement with an experiment-average single scattering albedo of 0.99 (−0.4, +1.0%). Of the submicron ionic mass, $80 \pm 10\%$ was sea salt, $16 \pm 8\%$ was non-sea-salt sulfate, and $4 \pm 3\%$ was methanesulfonate. Sea salt composed $99 \pm 0.7\%$ of the supermicron ionic mass. The magnitude of scattering by both submicron and supermicron aerosol was controlled by sea salt. The backscattered fraction for the submicron aerosol averaged 0.11 ± 0.02 and was controlled by the tailing of coarse mode sea-salt mass into the submicron size range. Calculated mass scattering efficiencies for submicron non-sea-salt sulfate ion averaged $1.5 \pm 0.74 \text{ m}^2 \text{ g}^{-1}$ (at 30 to 45% relative humidity) with the highest values corresponding to continentally influenced air masses where sulfate aerosol surface mean diameters and surface area concentrations were the largest. Mass scattering efficiencies for submicron sea salt were higher (averaging $4.2 \pm 0.96 \text{ m}^2 \text{ g}^{-1}$) due to the tailing of coarse mode sea salt into the particle size range most efficient for light scattering. Given the similar lifetimes of submicron non-sea-salt sulfate and sea salt in the marine boundary layer, it is evident that sea salt controls the aerosol optical properties in this Southern Ocean region.

1. Introduction

The scattering and absorption of solar radiation by both natural and anthropogenic tropospheric aerosol particles affect the Earth's radiation budget [Charlson *et al.*, 1991; Penner *et al.*, 1992; Sokolik and Toon, 1996]. The effects due to anthropogenic aerosol are

defined as climate forcings as they are an externally imposed change on the planetary heat balance. To determine the extent of the climate forcing resulting from anthropogenic aerosol, the optical properties and the factors controlling them must be well defined for both natural and anthropogenic aerosol systems. To establish the properties of a natural aerosol system, the First Aerosol Characterization Experiment (ACE 1) was conducted in the Southern Ocean south of Australia, a remote marine region where the aerosol is expected to be minimally perturbed by anthropogenic and continen-

Copyright 1998 by the American Geophysical Union.

Paper number 97JD02345.
0148-0227/98/97JD-02345\$09.00

tal sources. The experiment took place from November 15 to December 14, 1995, and involved two land-based sites (Cape Grim, Tasmania, and Macquarie Island), two ships (Australian R/V *Southern Surveyor* and the NOAA R/V *Discoverer*), and one airplane (NCAR C-130). The *Discoverer*'s study area extended from 41°S to 54°S between 135°E and 160°E.

The amount of incoming solar radiation that is scattered by the aerosol depends strongly on the particle size distribution. For a given aerosol mass concentration, the most efficient size range for scattering occurs between about 0.2 and 1.0 μm in particle diameter. The angular distribution of the scattered light intensity also varies with size. As a result, the hemispheric backscattered fraction, b , is maximal at diameters less than 0.3 μm , has a minimum near 0.5 μm , and a second smaller maximum between 1 and 2 μm .

Atmospheric aerosol usually consists of several modes with the accumulation mode occurring between about 0.1 and 1.0 μm which is the size range most efficient for scattering. Therefore aerosol chemical components that reside within the accumulation mode will have a significant impact on the scattering properties of the total aerosol. The extent of the impact will depend on the mean diameter and mass concentration of the component. The coarse mode peaks well outside of this size range but often has such a large mass concentration that it tails into the accumulation mode. As a result, a coarse mode aerosol chemical component also may significantly affect the scattering properties of the total aerosol.

Scattering and absorption of solar radiation by the aerosol also depend on the particle refractive index, density, and hygroscopicity which are a function of chemical composition. The dominant aerosol chemical components in the remote marine boundary layer are non-sea-salt (nss) SO_4^{2-} and sea salt. Non-sea-salt SO_4^{2-} aerosol is neutralized to a varying extent by reaction with gas phase NH_3 to form ammoniated sulfate salts such as NH_4HSO_4 and $(\text{NH}_4)_2\text{SO}_4$. Impactor measurements indicate that nss SO_4^{2-} aerosol mass resides primarily within the accumulation mode [e.g., *Whitby, 1978; Savoie and Prospero, 1982; Pszenny et al., 1989; Quinn et al., 1993*]. The majority of the sea-salt aerosol mass is found in the coarse mode but has been reported on occasion to dominate the mass concentration of the accumulation mode size range as well [*O'Dowd and Smith, 1993; Quinn et al., 1996*]. Other aerosol chemical components that may be present in much smaller quantities include methanesulfonate (MSA) which results from the atmospheric oxidation of dimethylsulfide, mineral dust, organic carbon species, and, to a lesser extent, elemental carbon.

Measurements made onboard the NOAA R/V *Discoverer* during ACE 1 allow for the determination of the influence of these three factors (particle size distribution, concentrations in the accumulation and coarse modes, and chemical composition in the accumulation

and coarse modes) on marine boundary layer (MBL) aerosol optical properties. Presented here are observations at a wavelength of 550 nm of the MBL scattering coefficient, σ_{sp} , for the submicron ($D_p < 1.0 \mu\text{m}$) and supermicron aerosol ($1.0 < D_p < 10 \mu\text{m}$); the ratio of the hemispheric backscattering coefficient to total scattering coefficient, $b = \sigma_{\text{bsp}}/\sigma_{\text{sp}}$; and the single scattering albedo, ω_0 . Also presented is the Ångström exponent, \AA , for the 450 and 700 nm wavelength pair. Each parameter is discussed in the context of the measured particle size distribution and chemical composition. In addition, measured number size distributions and chemical composition have been coupled with a Mie scattering model to estimate the contribution of the dominant aerosol chemical components to scattering and backscattering by the total aerosol. Using these model results, backscattered fractions and mass scattering efficiencies have been calculated for nss sulfate and sea-salt aerosol. A companion paper by *Bates et al.* [this issue], which also is based on measurements made on board the *Discoverer*, describes processes controlling the distribution of aerosol particles in the MBL.

2. Methods

2.1. Measurements

2.1.1. Aerosol sample inlet. Sample air for all measurements was drawn through a 6-m sample mast. The entrance to the mast was 18 m above sea level (asl) and 10 m forward of the ship's stack. To maintain isokinetic flow and minimize the loss of supermicron particles, the inlet was rotated into the relative wind. Air entered the inlet through a 5-cm diameter hole, passed through an expansion cone, and then into the 20-cm diameter sampling mast that had a length of 6 m. The flow through the mast was $1 \text{ m}^3 \text{ min}^{-1}$. The last 1.5 m of the mast were heated to establish a low reference relative humidity (RH) for the sample air of 30 to 45% (hereafter referred to as the instrumental RH). Individual 1.9 cm diameter stainless steel tubes extended into the heated portion of the mast. These were connected to the various aerosol instruments with carbon-embedded conductive tubing to prevent the loss of particles through static charging. Air was sampled only when the concentration of particles greater than 15 nm in diameter indicated the sample air was free of contamination, the relative wind speed was greater than 3 m s^{-1} , and the relative wind direction was forward of the beam.

2.1.2. Aerosol number size distribution. The number size distribution between 0.02 and 0.57 μm was measured every 10 min with a differential mobility particle sizer (DMPS) at an RH of 10%. The mobility distribution from the DMPS was inverted to a number distribution by assuming that a Fuchs-Boltzman charge distribution resulted from the Kr^{85} charge neutralizer (model 3077, TSI Inc.). The number distribution between 0.85 and 9.6 μm was measured with an aero-

dynamic particle sizer (APS) at an RH of 30 to 45%. Data at diameters larger than 5 μm were discarded due to interference from phantom counts. APS diameters were converted to geometric diameters by dividing by the square root of the particle density. Densities were calculated from the chemical equilibrium model AeRho which is based on measured chemical composition (see section 2.2.1). To align the DMPS and APS size distributions, DMPS diameters were grown to the RH of the air sampled by the APS using growth factors derived from the humidity-controlled tandem differential mobility analyzer (H-TDMA) [Berg *et al.*, this issue]. An average growth factor of 1.2 was used for nss SO_4^- and 1.5 for sea salt. The measured number size distributions were converted to surface area size distributions.

An interactive routine was used to fit lognormal curves to the different modes of the surface area size distributions. The coarse aerosol was fit with two lognormal modes as one mode did not accurately represent the mean diameter as well as the geometric standard deviation of the aerosol in this size range. This follows O'Dowd *et al.* [1997] who suggest that different production mechanisms generate several modes within the coarse size fraction. The modal parameters of geometric surface mean diameter, D_{gs} (μm); total surface area concentration, S ($\mu\text{m}^2 \text{ cm}^{-3}$); and geometric standard deviation, σ_{sg} , were calculated for each mode. The geometric surface mean diameter reported for the coarse aerosol is that of the smallest of the two modes, while the surface area concentration is the sum of the two modes.

2.1.3. Size dependent aerosol ionic composition. Seven-stage multijet cascade impactors sampling air at 30 to 45% RH [Bernier *et al.*, 1979] were used to determine the mass size distributions of Cl^- , Br^- , NO_3^- , SO_4^- , MSA^- , Na^+ , NH_4^+ , K^+ , Mg^{2+} , and Ca^{2+} . The 50% aerodynamic cutoff diameters, $D_{50,\text{aero}}$, were 0.27, 0.37, 0.64, 1.2, 2.3, 4.7, and 12 μm . For comparison to measurements of the number size distribution, the impactor aerodynamic diameters were converted to geometric diameters by dividing by the square root of the particle density. All impactor results are plotted as $\Delta m / \Delta \log D_p$ versus \log of geometric particle diameter at the instrumental RH of 30 to 45%.

The impaction stage at the inlet of the impactor was covered with silicone grease to prevent the bounce of large particles onto the downstream stages. Tedlar films were used on the six largest stages of the impactor, and a Millipore Fluoropore filter (1.0- μm pore size) was used for the smallest stage. Films were cleaned in an ultrasonic bath in 10% H_2O_2 for 30 min, rinsed in distilled, deionized water, and dried in an NH_3 - and SO_2 -free glove box. All handling of the substrates was done in the glove box. Blank levels were determined by loading an impactor with substrates and deploying it at the sampling site for the length of a typical sampling period without drawing any air through it. On average, the percent blank to sample ratios were as follows: Na^+

$= 17\%$, $\text{NH}_4^+ = 40\%$, $\text{K}^+ = 30\%$, $\text{Mg}^{2+} = 18\%$, $\text{Ca}^{2+} = 60\%$, $\text{Cl}^- = 20\%$, $\text{Br}^- = 25\%$, $\text{NO}_3^- = 40\%$, and $\text{SO}_4^- = 9\%$. MSA^- blanks were below the detection limit.

After sample collection, the material on the substrates was extracted by first wetting with 1 mL of methanol and then adding 5 mL of distilled deionized water and sonicating for 30 min. The extracts were analyzed within 1 to 2 days of sample collection by ion chromatography. The cation analysis was done with a Dionex CS-12 column, 20-mM MSA^- eluant, and deionized water regenerant using the Dionex CSRS-1 suppressor system. Anion analysis was done with a Dionex AS-4A column, 0.76-mM NaHCO_3 /2.0-mM Na_2CO_3 eluant, and 12.6-mM H_2SO_4 regenerant. MSA^- analysis was performed with a Dionex AS-4 column and a stepwise elution with 5-mM NaOH eluant followed by 100-mM NaOH eluant, and a 12.6-mM H_2SO_4 regenerant. Non-sea-salt sulfate concentrations were calculated from Na^+ concentrations and the ratio of sulfate to sodium in seawater.

2.1.4. Size dependent aerosol total mass. Submicron and supermicron aerosol mass were determined gravimetrically [see Quinn and Coffman, this issue]. Samples were collected with a two-stage impactor with size cuts of $D_{50,\text{aero}} = 1.0 \mu\text{m}$ and $D_{50,\text{aero}} = 10 \mu\text{m}$. (A D_{aero} of 1.0 μm is approximately equal to a geometric diameter of 0.81 μm , and a D_{aero} of 10 μm is approximately equal to a geometric diameter of 8 μm). A 47-mm Millipore Fluoropore filter (1.0- μm pore size) was used for the submicron stage, and a 90-mm Tedlar impactor film was used for the supermicron stage. Filters and films were weighed at the Pacific Marine Environmental Laboratory (PMEL) before and after sample collection with a Mettler UMT2 and Cahn Model 29 microbalance, respectively. The microbalances were housed in a glove box kept at a humidity of $33 \pm 2\%$. Room air was passed through a scrubber of activated charcoal, potassium carbonate, and citric acid to remove gas phase organics, acids, and ammonia. The scrubbed air was circulated through a flat baffle box containing a saturated solution of $\text{MgCl}_2 \cdot 6\text{H}_2\text{O}$ and then through the glove box [Young, 1967; McInnes *et al.*, 1996]. Static charging, which can result in balance instabilities, was minimized by coating the walls of the glove box with a static dissipative polymer (Tech Spray, Inc.), placing an antistatic mat on the glove box floor, using antistatic gloves while handling the substrates, and exposing the substrates to a ^{210}Po source.

2.1.5. Gas phase ammonia. A tandem sampling system was used to determine gas phase ammonia concentrations [Quinn *et al.*, 1990]. A cyclone separator removed large sea-salt particles. The cyclone was followed by a 47-mm Millipore Fluoropore filter for the collection of the remaining particles and 4 Whatman 41 paper filters in series coated with 0.01 M oxalic acid for the collection of NH_3 (g). Three tandem sampling systems were deployed at once, two for samples and one for a blank. The blank followed the samples through the

entire sampling and analysis procedure but had no air flow drawn through it. The Whatman filters were extracted with 5 mL of distilled deionized water and were sonicated for 15 min. The extracts were analyzed by ion chromatography. All sample handling was carried out in the NH_3 -free glove box. On average, the blank concentration was 18% of the sample concentration.

2.1.6. Measured scattering, backscattering, and absorption coefficients. Measurements of the aerosol scattering and backscattering coefficients were made with an integrating nephelometer (Model 3563, TSI Inc.) at wavelengths of 450, 550, and 700 nm. Values of the scattering and backscattering coefficient are reported at 550 nm, while the Ångström exponent, α , is reported for the 450 and 700 nm wavelength pair. Two single-stage cascade impactors, one having a $D_{50,\text{aero}}$ of 1.0 μm and the other 10 μm , were placed upstream of the nephelometer. A valve switched between the two impactors every 15 min so that sampling alternated between submicron aerosol and all aerosol with $D_{\text{aero}} < 10 \mu\text{m}$. Scattering and backscattering by the supermicron aerosol was determined by difference.

The nephelometer measures scattering and backscattering by integrating over zenith angle θ . Ideal limits of integration are 0° to 180° for scattering and 90° to 180° for backscattering. Because of geometrical limitations (the sensing volume is not infinitely long), the actual limits of integration within the nephelometer are truncated. The angular truncation error is most pronounced for supermicron particles. Additional uncertainties for the supermicron size range result from inlet losses. To improve the estimation of the actual scattering and backscattering by particles, measured values were multiplied by the ratio of the Mie-calculated true scattering ($\sigma_{\text{sp-T}}$) to the true scattering modified to simulate the nephelometer response ($\sigma_{\text{sp-Nsim}}$) so that for the scattering coefficient,

$$\sigma_{\text{sp}} = \sigma_{\text{sp-meas}} \times \frac{\sigma_{\text{sp-T}}}{\sigma_{\text{sp-Nsim}}} \quad (1)$$

The Mie calculations are described in more detail in section 2.2.2. On average, values of $\sigma_{\text{sp-T}} / \sigma_{\text{sp-Nsim}}$ were 1.07 ± 0.02 and 1.3 ± 0.02 for the submicron and supermicron size ranges, respectively. Values of $\sigma_{\text{bsp-T}} / \sigma_{\text{bsp-Nsim}}$ were 0.95 ± 0.005 and 1.03 ± 0.01 for the submicron and supermicron size ranges, respectively.

Values of $\sigma_{\text{sp-T}}$ and $\sigma_{\text{bsp-T}}$ could have been used to represent the actual aerosol scattering and backscattering coefficients instead of the method shown in (1). The accuracy of this approach is limited, however, due to uncertainties associated with the measured number size distribution. Since APS values at diameters larger than 5 μm were discarded due to phantom counts, the uncertainty in this size range is large. Therefore (1) was used to preserve the information derived from the nephelometer and to take into account its nonideal behavior. The result is scattering and backscattering coefficients

as representative as possible of ambient values (for more details, see *Quinn and Coffman* [this issue]). The absorption coefficient for all aerosol with $D_{\text{aero}} < 10 \mu\text{m}$ was measured at 550 nm by monitoring the change in transmission through a filter with a Particulate Soot Absorption Photometer (PSAP, Radiance Research).

2.1.7. Ancillary parameters. Also measured were meteorological parameters including surface temperature, relative humidity, wind speed and direction, as well as vertical profiles of these parameters from rawinsondes. Air mass back trajectories and concentrations of ^{222}Rn [Whittlestone and Zahorowski, this issue] were used to determine the source of the sampled air masses. The air mass back trajectories were calculated for up to 5 days with the hybrid single-particle Lagrangian integrated trajectory model (NOAA HY-SPLIT 3.2. code [Drazler, 1992]) using the Australian Bureau of Meteorology Global Atmospheric Sampling Program (GASP) model (S. T. Siems et al., unpublished manuscript, 1998). The model has approximately 5 degrees of horizontal resolution and 18 vertical levels.

2.2. Model Calculations

2.2.1. Calculation of size dependent particle density and refractive index. Particle density and refractive index as a function of size were estimated from AeRho, a chemical model based on thermodynamic equilibrium. The calculations were done at the instrumental RH of 30 to 45% for each size bin of the impactor using the measured impactor ion concentrations (in nmol m^{-3} of air) and the RH and temperature of the sampled air stream as input data. The model is based on the assumption of an external mixture of nss sulfate and sea-salt aerosol. The nss sulfate aerosol is composed of SO_4^{2-} and associated NH_4^+ and H_2O mass, and the sea-salt aerosol is composed of Na^+ , Cl^- , sea-salt SO_4^{2-} , and associated H_2O mass.

The steps of the model are shown in Figure 1. The chemical reactions allowed to occur in the nss sulfate/sea salt aerosol system are shown in Table 1. The ionic molalities for each of the input species are determined initially by assuming that the activity of water is equal to the instrumental RH. Then, using the ZSR method [Zdanovskii, 1936; Robinson and Stokes, 1965], a further approximation of the water content of the aerosol is made. Aqueous phase concentrations are activity corrected using the method of Bromley [1973] which allows for the prediction of activity coefficients of strong electrolytes in multielectrolyte solutions based on binary solution activity coefficients [Piliinis and Seinfeld, 1987; Quinn et al., 1992]. The pure-solution binary activity coefficients are calculated using the method of Pitzer and Mayorga [1973]. The ionic species are partitioned between the solid and aqueous phases with the solids precipitating in the most thermodynamically favorable order. The crystallization humidities that are used are listed in Table 1. The remaining aqueous ionic

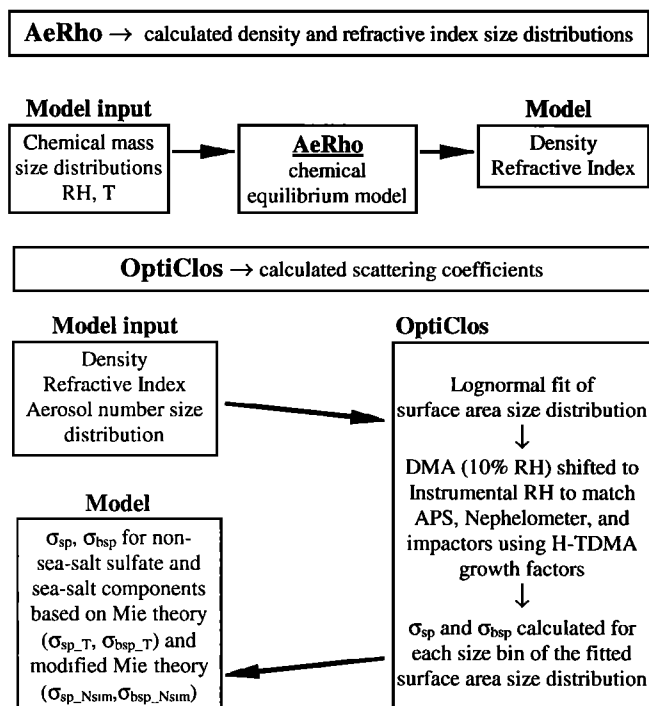


Figure 1. Steps in the chemical thermodynamic equilibrium model, AeRho, used to calculate particle density and refractive index as a function of size and the Mie scattering model, OptiClos, used to calculate scattering and backscattering coefficients of the aerosol chemical components at a wavelength of 550 nm. An unmodified Mie integral was used to calculate the true scattering ($\sigma_{sp,T}$) and backscattering ($\sigma_{bsp,T}$) coefficients. A Mie integral modified to simulate the nephelometer response was used to calculate nephelometer simulated values of $\sigma_{sp,Nsim}$ and $\sigma_{bsp,Nsim}$.

species are converted to aqueous compounds in accordance with the thermodynamic equilibrium constants. Finally, thermodynamic equilibrium with respect to water is tested for, and the water activity is iterated until equilibrium is established.

By assuming thermodynamic equilibrium, AeRho is able to provide the molecular composition necessary for estimating particle density and refractive index as a function of particle size. Measurements have shown, however, that metastable particles can exist in the atmosphere [Rood *et al.*, 1989]. Therefore polynomial fits based on data of Tang and Munkelwitz [1991, 1994] for metastable particles are used to estimate densities of individual species. Data from Bray [1970] are used to estimate the density of H_2SO_4 . A volume-weighted average is taken of the density of the individual species to estimate the density of each impactor size bin. The method of partial molar refraction [Stelson, 1990] is used to estimate the refractive index of each size bin.

2.2.2. Calculation of scattering and backscattering coefficients of the aerosol chemical components. The aerosol is assumed to be externally mixed such that the accumulation and coarse modes derived from the lognormal fit of the surface area size distribu-

tion are composed of pure nss SO_4^{2-} and sea-salt aerosol, respectively. Given that the measured and calculated submicron scattering and backscattering coefficients agree within $\pm 20\%$, which is within the uncertainty of the methods, this assumption appears to be adequate (see Quinn and Coffman [this issue] for more information). In any case, if the aerosol is internally mixed to some degree, it is not likely to change the overall result of the component scattering calculations presented below.

Using the OptiClos model (Figure 1), a scattering (or backscattering) size distribution was calculated for the accumulation and coarse modes using the refractive index from AeRho and scattering efficiencies at 550 nm based on Mie theory [Bohren and Huffman, 1983]. The scattering and backscattering efficiencies are obtained at discrete particle sizes by integrating over the scattered intensity function from 0° to 180° and 90° to 180° , respectively. The resulting scattering (backscattering) coefficients are summed to produce integral values for the accumulation and coarse modes. Through a similar summation process, integral values are calculated for the submicron and supermicron size fractions.

A Mie integral modified to simulate the nephelometer response was used to calculate the nephelometer-simulated particle scattering and backscattering coefficients, $\sigma_{sp,Nsim}$ and $\sigma_{bsp,Nsim}$. Measured sensitivity functions were used to account for the truncation of integration angles and wavelength nonidealities [Heintzenberg, 1978; Anderson *et al.*, 1996].

The measured submicron and supermicron scattering and backscattering coefficients then were partitioned between the nss SO_4^{2-} and sea-salt components as follows. For the submicron size fraction of component j

$$\sigma_{sp,sub,j} = \sigma_{sp,sub} \times \frac{\sigma_{sp,T,sub,j}}{\sigma_{sp,T,sub}} \quad (2)$$

where $\sigma_{sp,sub}$ is derived from (1), $\sigma_{sp,T,sub,j}$ is the Mie-calculated true scattering due to submicron component j , and $\sigma_{sp,T,sub}$ is the Mie-calculated true scattering due to the sum of submicron nss SO_4^{2-} and sea salt.

3. Results

3.1. Physical Properties of the Accumulation and Coarse Modes

Factors affecting accumulation mode values of the geometric surface mean diameter ($D_{gs,acc}$) and surface area concentration (S_{acc}) include the origin of the aerosol and the length of time it spends in the boundary layer. Continentally derived aerosol within this size range can be transported over long distances to the marine atmosphere resulting in large values of S_{acc} relative to those of unperturbed marine aerosol [e.g., Quinn *et al.*, 1990; Clarke, 1993]. MBL residence times of up to several days allow for vapor condensation onto and cloud processing of the aerosol and therefore result in

Table 1. Chemical Reactions Included in AeRho, the Thermodynamic Chemical Equilibrium Model of the nss Sulfate/Sea-Salt Aerosol System, Which Was Used to Calculate the Aerosol Density and Refractive Index for Each Impactor Size Bin

Crystallization RH, %	
<i>Aqueous Reactions</i>	
$\text{Na}_2\text{SO}_4 (\text{aq}) \leftrightarrow 2\text{Na}^+ (\text{aq}) + \text{SO}_4^{2-} (\text{aq})$	
$\text{NH}_4\text{HSO}_4 (\text{aq}) \leftrightarrow \text{NH}_4^+ (\text{aq}) + \text{HSO}_4^- (\text{aq})$	
$(\text{NH}_4)_2\text{SO}_4 (\text{aq}) \leftrightarrow 2\text{NH}_4^+ (\text{aq}) + \text{SO}_4^{2-} (\text{aq})$	
$\text{NaHSO}_4 (\text{aq}) \leftrightarrow \text{Na}^+ (\text{aq}) + \text{HSO}_4^- (\text{aq})$	
$\text{HCl} (\text{aq}) \leftrightarrow \text{H}^+ (\text{aq}) + \text{Cl}^- (\text{aq})$	
$\text{NH}_4\text{Cl} (\text{aq}) \leftrightarrow \text{NH}_4^+ (\text{aq}) + \text{Cl}^- (\text{aq})$	
$\text{NaCl} (\text{aq}) \leftrightarrow \text{Na}^+ (\text{aq}) + \text{Cl}^- (\text{aq})$	
$\text{H}_2\text{SO}_4 (\text{aq}) \leftrightarrow \text{HSO}_4^- (\text{aq}) + \text{H}^+ (\text{aq})$	
$\text{HSO}_4^- (\text{aq}) \leftrightarrow \text{H}^+ (\text{aq}) + \text{SO}_4^{2-} (\text{aq})$	
<i>Solid Phase Reactions</i>	
$\text{Na}_2\text{SO}_4 (\text{s}) \leftrightarrow 2\text{Na}^+ (\text{aq}) + \text{SO}_4^{2-} (\text{aq})$	59
$(\text{NH}_4)_2\text{SO}_4 (\text{s}) \leftrightarrow 2\text{NH}_4^+ (\text{aq}) + \text{SO}_4^{2-} (\text{aq})$	40
$\text{NH}_4\text{Cl} (\text{s}) \leftrightarrow \text{NH}_4^+ (\text{aq}) + \text{Cl}^- (\text{aq})$	40
$\text{NaCl} (\text{s}) \leftrightarrow \text{Na}^+ (\text{aq}) + \text{Cl}^- (\text{aq})$	25
$\text{NaHSO}_4 (\text{s}) \leftrightarrow \text{Na}^+ (\text{aq}) + \text{HSO}_4^- (\text{aq})$	22

Crystallization RH values were taken from *Tang and Munkelwitz* [1994] except that of NaCl which is based on laboratory studies.

aerosol growth and an increase in S_{acc} [e.g., *Hoppel et al.*, 1986, 1994; *Quinn et al.*, 1996; *Bates et al.*, this issue]. Here the MBL residence time of an air parcel and the aerosol it contains is defined as the length of time the parcel spends below 900 mbar prior to being sampled on the ship. This residence time was estimated from the calculated back trajectories.

The portion of the sea salt or coarse mode considered here, as determined by the size range measured by the APS and the impactors, extends up to diameters of 5 to 10 μm . The mean diameter ($D_{\text{gs,cs}}$), surface area concentration (S_{cs}), and vertical distribution of this size range are a function of the surface source or wind speed, vertical and horizontal mixing, and removal by dry and wet deposition and gravitational settling. A correspondence of increased wind speed and sea-salt number concentration has been reported for a number of size ranges [e.g., *Gathman*, 1983; *Smith et al.*, 1989; *O'Dowd and Smith*, 1993; *Bates et al.*, this issue]. The correlation may not always be statistically robust, however, due to the influence of mixing within the MBL and removal processes [*Mestayer et al.*, 1996]. Indeed, model results indicate that the concentration of small sea-salt particles ($D_p < 0.6 \mu\text{m}$) is less dependent on wind speed than that of large particles ($D_p > 8 \mu\text{m}$) due to their longer residence time [*Gong et al.*, 1997]. With a longer residence time (up to 2.5 days), particle concentration is controlled by vertical and horizontal mixing and nonsedimentation removal processes in addition to the local wind speed.

Time series of D_{gs} and S for the accumulation and coarse modes during ACE 1 are shown in Figure 2 for the instrumental RH (30 to 45%). Ancillary parameters that indicate the origin and history of the sampled aerosol (wind speed, atmospheric pressure, rain rate, ^{222}Rn , and σ_{ap}) are shown in Figure 3.

$D_{\text{gs,acc}}$ averaged $0.20 \mu\text{m} \pm 20\%$ and S_{acc} averaged $6.5 \mu\text{m}^2 \text{cm}^{-3} \pm 66\%$. Larger values of $D_{\text{gs,acc}}$ and S_{acc} were found in air masses that had passed over Australia prior to being sampled (day of year (DOY) 329.8 to 330.5, 331.5 to 332.2, 333 to 333.25, and 342.7 to 343.4). These air masses, designated here as perturbed marine, were marked by elevated ^{222}Rn concentrations ($>100 \text{ mBq m}^{-3}$) and calculated back trajectories that indicated transport of air from the continent. During one additional period (DOY 335.5 to 336), high levels of $D_{\text{gs,acc}}$ were observed accompanied by low ^{222}Rn concentrations but high σ_{ap} values. In this case, calculated back trajectories indicated the sampled air mass had spent greater than 5 days in the MBL with possible transport from Madagascar.

Elevated, above average values of $D_{\text{gs,acc}}$ and S_{acc} also were associated with marine aerosol that had spent 5 or more days in the MBL prior to reaching the ship (DOY 340 to 341). Here marine aerosol refers to aerosol associated with air masses having southwest trajectories, low ^{222}Rn ($<100 \text{ mBq m}^{-3}$), and low σ_{ap} values ($<0.25 \text{ Mm}^{-1}$). During this period, a high pressure system was developing preventing the passage of fronts into the ACE region. This is in contrast to other pe-

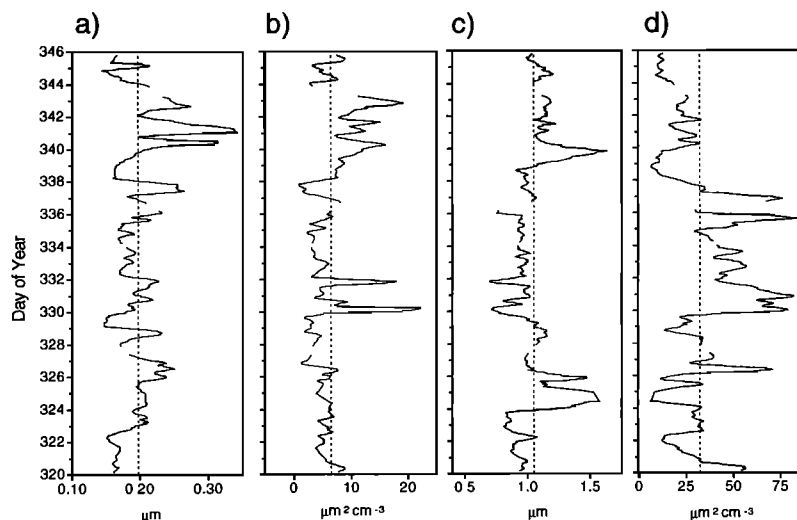


Figure 2. Shown as a function of day of year are 6-hour running averages of the modal parameters for the surface area size distribution at instrumental RH (30 to 45%) including (a) accumulation mode geometric surface mean diameter, $D_{gs,acc}$; (b) accumulation mode total surface area concentration, S_{acc} ; (c) coarse mode $D_{gs,cs}$; and (d) coarse mode S_{cs} . Mean values are indicated by the dashed line. Parameters are based on the fitting of a series of lognormal curves to the size distribution. The coarse aerosol was fit with two lognormal curves. Reported values of $D_{gs,cs}$ are for the smaller of the two modes, while S_{cs} is a sum for the two modes.

riods in the first 10 days of the experiment when the aerosol was marine but spent less time in the MBL due to repeated frontal passages [Hainsworth *et al.*, this issue].

$D_{gs,cs}$ averaged $1.0 \mu\text{m} \pm 19\%$. The standard deviation of the average of $D_{gs,cs}$ is similar in magnitude to the uncertainty associated with its derivation from the interactive fitting program. S_{cs} was more variable averaging $32 \mu\text{m}^2 \text{cm}^{-3} \pm 62\%$. A general correspondence was observed between low local wind speed and low S_{cs} (DOY 321.75 to 322.5, 324.3 to 324.8, 328 to 329.5, and 338 to 340) and high local wind speed and

high S_{cs} (DOY 326.25 to 326.7, 329.8 to 330.5, 330.5 to 331, and 332.25 to 334).

3.2. Chemical Properties of the Accumulation and Coarse Modes

A mass closure experiment was performed in which mass derived from gravimetric analysis was compared to the ionic mass derived from ion chromatography analysis (Quinn and Coffman, this issue). This comparison allows for the determination of the fraction of the total aerosol mass that is composed of water soluble ionic species. On the basis of results from two-stage impactors, ionic species and associated water mass accounted for nearly 100% of the mass in both the submicron and supermicron size fractions.

The ionic mass was dominated by nss SO_4^{2-} aerosol (considered here and throughout the paper to be the sum of sulfate, ammonium, and associated water), sea-salt aerosol, and, to a lesser extent, methanesulfonate. As shown in Figure 4a, the majority ($75 \pm 30\%$) of the nss SO_4^{2-} mass was found in the submicron size range where concentrations ranged from 0.08 to $0.3 \mu\text{g m}^{-3}$ and averaged $0.16 \pm 0.07 \mu\text{g m}^{-3}$. Highest concentrations corresponded to continentally influenced air masses (DOY 329.8 to 330.5, 331.5 to 332.2, 335.5 to 336.0, and 342.7 to 343.4) and to marine air masses that had spent 5 or more days in the MBL (DOY 322 to 323 and 338 to 341) (see Figure 11a for absolute concentrations of nss SO_4^{2-} ion in the submicron size range).

Concentrations of sea-salt aerosol mass were much larger, ranging from 3 to $25 \mu\text{g m}^{-3}$ with the majority ($90 \pm 2\%$) occurring in the supermicron size range

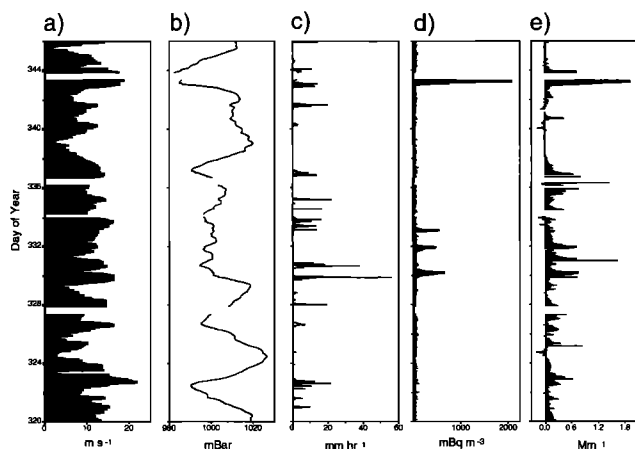


Figure 3. Shown as a function of day of year are 1-hour averages of (a) local wind speed, (b) atmospheric pressure, (c) rain rate, (d) ^{222}Rn concentrations, and (e) the aerosol absorption coefficient, σ_{ap} .

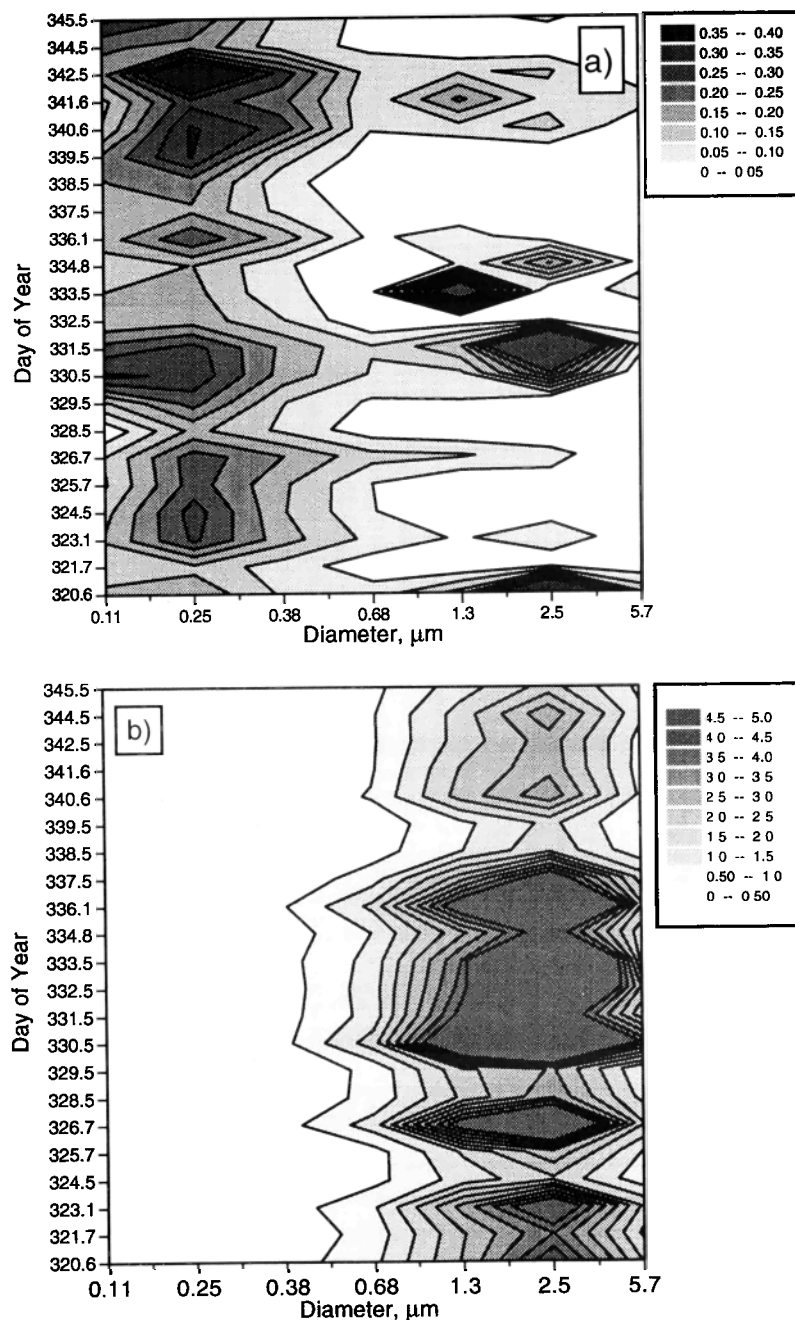


Figure 4. Contour plots of the mass size distribution, $\Delta m / \Delta \log D_p$ ($\mu\text{g m}^{-3} \mu\text{m}^{-1}$) as a function of day of year for (a) nss SO_4^{2-} ion, (b) Na^+ as an indicator of sea-salt aerosol and (c) MSA^- . (d) Size distribution of the NH_4^+ to nss SO_4^{2-} molar ratio. Distributions are shown in terms of the log of geometric particle diameter at the instrumental RH of 30 to 45%. The y scale corresponds to the midpoint of each impactor sampling period.

(Figure 4b). To determine the degree to which the local wind speed controlled the sea-salt mass concentration, a log linear fit $[\ln(m_{\text{sea salt}}) = \ln(b) + aU]$ was applied to the measured sea-salt mass concentration ($m_{\text{sea salt}}$) and local wind speed (U). Local wind speed values were averaged over the 12- to 24-hour time periods of the impactor samples.

A regression with the submicron sea-salt mass concentration resulted in a coefficient of determination, r^2 ,

of 0.42, slope of 0.13, and y intercept of 0.4. Using the supermicron sea-salt mass resulted in values of $r^2 = 0.41$, $a = 0.14$, and $b = 2.9$. The r^2 value of 0.4 indicates that about 40% of the variance in the sea-salt mass concentration can be explained by the local wind speed. The lifetime of up to a couple of days associated with this size range ($0.1 < D_p < 10 \mu\text{m}$) results in the influence of other factors on the mass concentration including advection and vertical mixing. The slope of

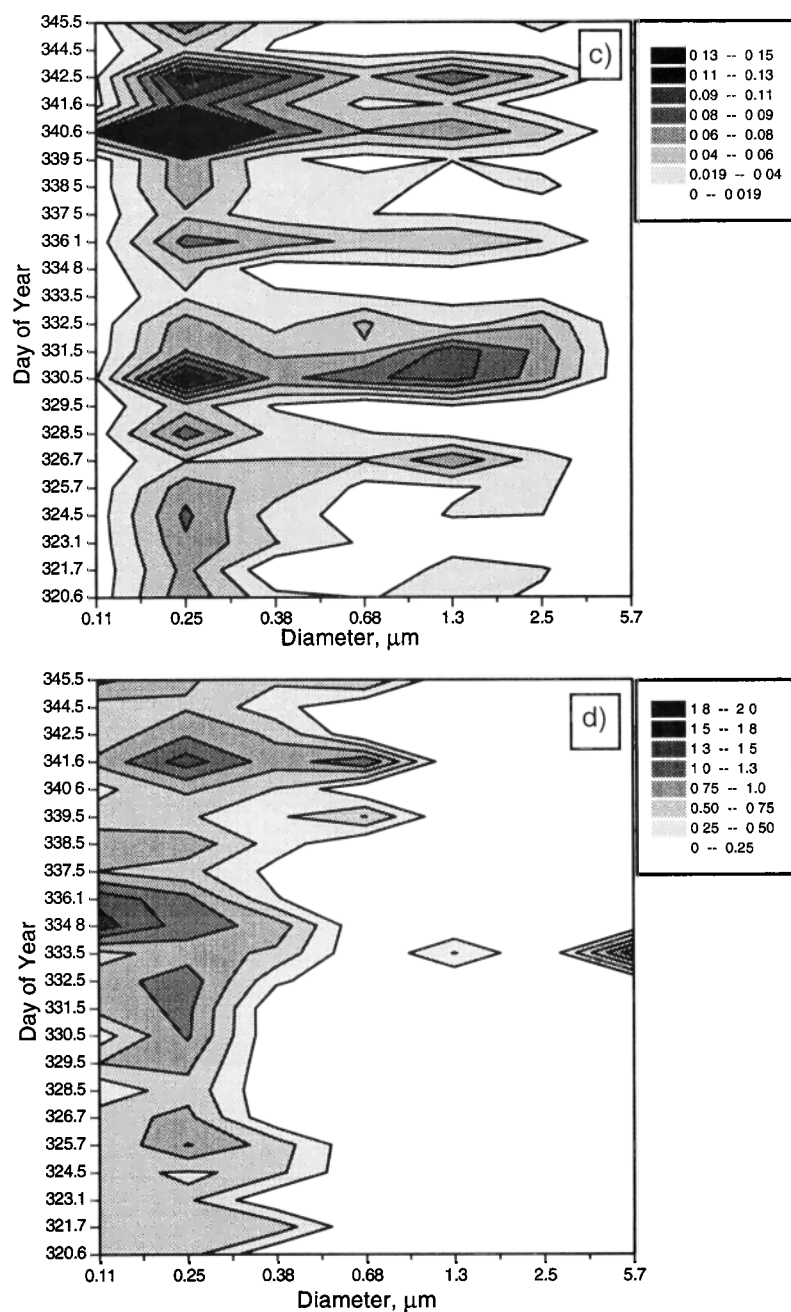


Figure 4. (continued)

0.13 to 0.14 agrees in general with values reported for a variety of oceanic regions [e.g., *Gong et al.*, 1997] and in particular with values reported for Cape Grim by *Gras and Ayers* [1983] (slope equal to 0.124 and y intercept equal to 2.52).

MSA concentrations ranged from 0.02 to $0.2 \mu\text{g m}^{-3}$ with an average of 70% occurring in the submicron size range (Figure 4c). The highest coarse mode concentrations and, consequently, most bimodal MSA size distributions were observed in both perturbed marine and marine air masses having MBL residence times of at least 5 days. The MSA to nss SO_4^- molar ratio in marine air masses for all particles less than $12 \mu\text{m}$ in diam-

eter was $24 \pm 16\%$. Submicron and supermicron aerosol ratios averaged $22 \pm 16\%$ and $63 \pm 77\%$, respectively. The submicron aerosol ratio is in good agreement with previously reported submicron values for Cape Grim during November and December [*Ayers et al.*, 1991].

NH_4^+ to nss SO_4^- molar ratios averaged 0.9 for particles with geometric diameters less than $0.25 \mu\text{m}$ and 0.3 for diameters between 0.25 and $0.68 \mu\text{m}$ (Figure 4d) indicating that low gas phase NH_3 concentrations resulted in only partially neutralized nss SO_4^- aerosol. AeRho, a chemical equilibrium model, was used to check for the existence of equilibrium between the gas and particle phases with respect to NH_3 . The predicted equilib-

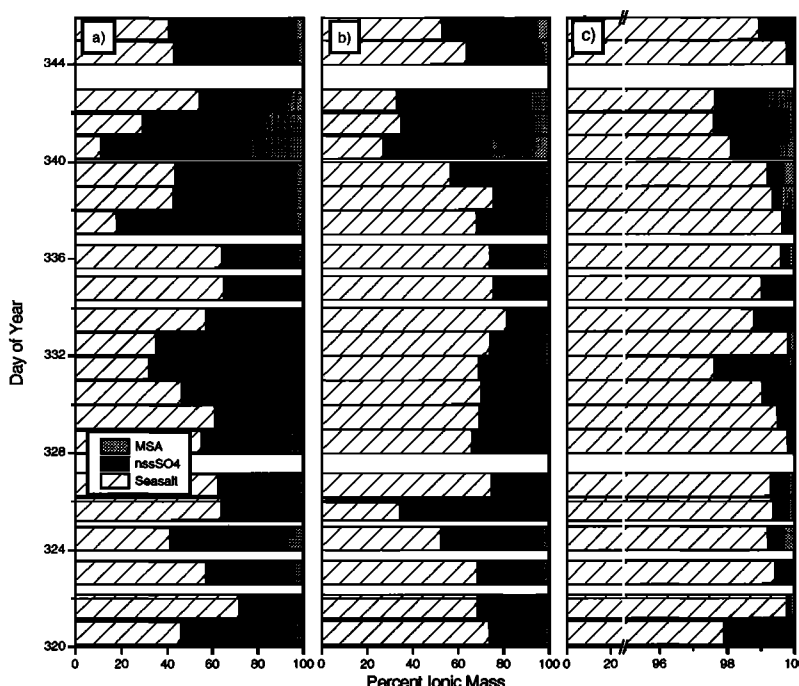


Figure 5. Ionic mass fractions of nss SO_4^- , sea salt, and methanesulfonate aerosol for (a) geometric $D_p < 0.25 \mu\text{m}$ (instrumental RH), (b) $0.25 < D_p < 0.38 \mu\text{m}$, and (c) $0.38 < D_p < 10 \mu\text{m}$ (note axis break at 25%). The ionic mass fraction of an aerosol chemical component is defined as the fraction of the total aerosol mass derived from the ion chromatography analysis that is attributable to that component.

rium concentrations of NH_3 (g) agreed well with the 3 to 30 pptv values measured with oxalic acid coated filters. On the basis of this comparison, NH_3 appears to have been in equilibrium between these two atmospheric phases.

Ionic mass fractions (Figure 5) give an indication of the relative concentrations of the three major aerosol chemical components as a function of particle size. For particles with geometric diameters less than $0.25 \mu\text{m}$, $45 \pm 14\%$ of the ionic mass was nss SO_4^- aerosol, $47 \pm 16\%$ was sea salt, and $8 \pm 7\%$ was MSA. For geometric diameters between 0.25 and $0.38 \mu\text{m}$, the amount of nss SO_4^- aerosol was less ($32 \pm 12\%$), while concentrations of sea-salt aerosol were more ($62 \pm 16\%$), and MSA remained about the same ($6 \pm 5\%$). Sea salt was dominant in particles greater than $0.38 \mu\text{m}$ ($99 \pm 0.7\%$) with less than a percent attributable to nss SO_4^- and methanesulfonate aerosol.

3.3. Aerosol Optical Properties

3.3.1. Measured scattering and backscattering coefficients. To separate the scattering due to submicron and supermicron particles, an impactor ($D_{50,\text{aero}} = 1.0 \mu\text{m}$) was valved into the nephelometer sample line at 15-min intervals. This technique allows for a representative measure of the scattering by the submicron aerosol that is present in a well-mixed MBL. In addition, a correction was applied to the measured values to account for the angular truncation error of the nephelometer (section 2.1.6).

At the instrumental RH of 30 to 45% and a wavelength of 550 nm, the scattering coefficient, σ_{sp} , for the submicron aerosol ranged from 0.66 to 38 Mm^{-1} with an average and standard deviation of $4.4 \pm 3 \text{ Mm}^{-1}$, while values for the supermicron aerosol ranged from 1.7 to 130 Mm^{-1} with an average and standard deviation of $23 \pm 16 \text{ Mm}^{-1}$ (Figure 6). In general, highest values for both size ranges corresponded to periods of high local wind speeds indicating the influence of both submicron and supermicron sea-salt particles on scattering by the total aerosol ($r^2 = 0.4$ for local wind speed versus both submicron and supermicron σ_{sp}). The correlation is limited by the degree of control that the local wind speed has over the sea-salt concentration.

Measured hemispheric backscattering coefficients, σ_{bsp} , were about an order of magnitude lower than σ_{sp} ranging from near the detection limit (0.3 Mm^{-1} at 550 nm) to 5.0 Mm^{-1} for the submicron fraction and to 14 Mm^{-1} for the supermicron aerosol. This resulted in a hemispheric backscattered fraction for the submicron aerosol, b_{sub} , of 0.11 ± 0.02 and for the supermicron aerosol, b_{sup} , of 0.13 ± 0.01 (Figure 7).

3.3.2. Spectral dependence of the measured scattering coefficients. The Ångström exponent, \tilde{a} , describes the dependence of the aerosol light scattering coefficient on wavelength λ and therefore on particle size. Defined in terms of the measured σ_{sp} at $\lambda_1 = 0.7$ and $\lambda_2 = 0.45 \mu\text{m}$

$$\tilde{a} = -\frac{\log [\sigma_{\text{sp}}(\lambda_1) / \sigma_{\text{sp}}(\lambda_2)]}{\log [\lambda_1 / \lambda_2]} \quad (3)$$

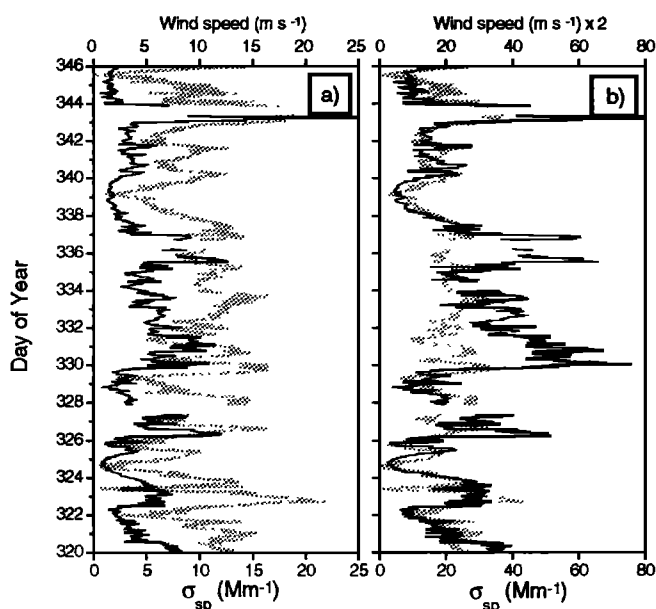


Figure 6. Measured scattering coefficient at 550 nm at instrumental RH (30 to 45%) as a function of day of year. One-hour average values are shown for (a) submicron aerosol with $D_{p,aero} < 1.0 \mu\text{m}$ (dark line) and (b) supermicron aerosol with $1.0 < D_{p,aero} < 10 \mu\text{m}$ (dark line). Also shown is the local wind speed in m s^{-1} (light line).

Physically, a shift of \hat{a} to more negative values indicates an increase in scattering at $0.7 \mu\text{m}$ relative to $0.45 \mu\text{m}$ due to the presence of relatively more large diameter particles and/or fewer small diameter particles. A shift to more positive values indicates an increase in scattering at $0.45 \mu\text{m}$ relative to $0.7 \mu\text{m}$ due to more small

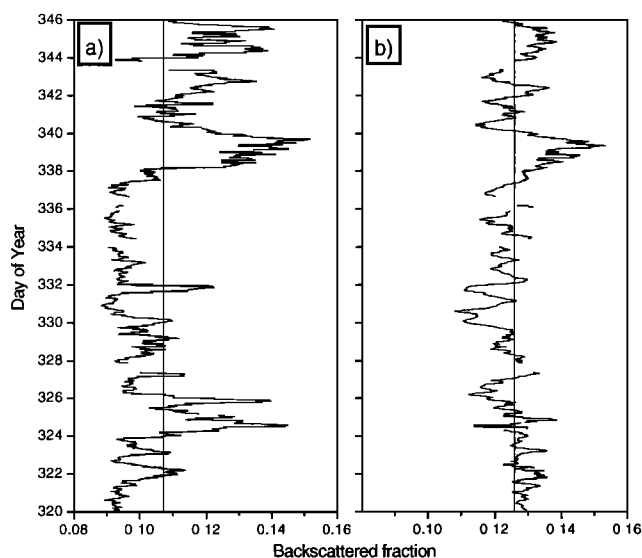


Figure 7. Measured hemispheric backscattered fraction at 550 nm and the instrumental RH (30 to 45%) as a function of day of year for (a) $D_{p,aero} < 1.0 \mu\text{m}$ and (b) $1.0 < D_{p,aero} < 10 \mu\text{m}$. Values are plotted as a 1.5-hour running mean average. Mean values are indicated by the straight line.

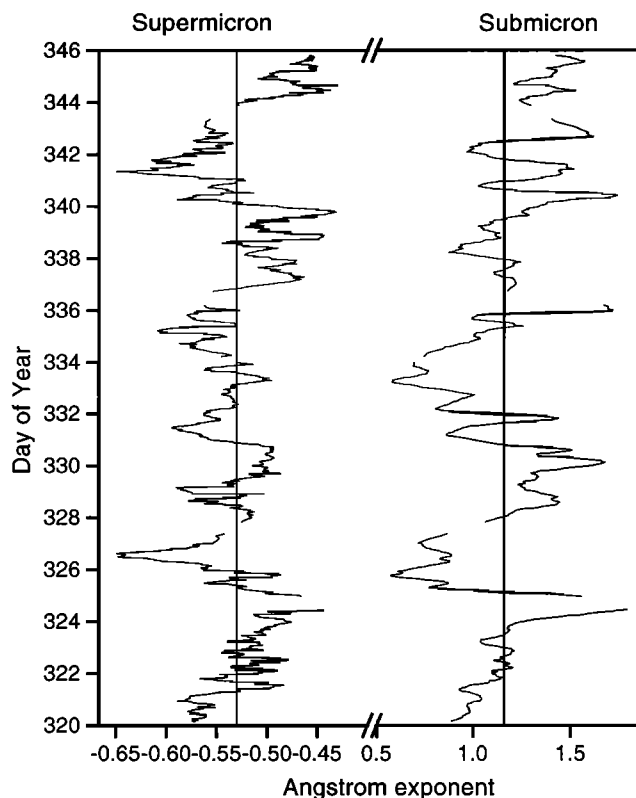


Figure 8. Six-hour running average of the Ångström exponent calculated from nephelometer measurements of the scattering coefficient at 450 and 700 nm. Values are shown for the submicron aerosol with $D_{p,aero} < 1.0 \mu\text{m}$ and the supermicron aerosol with $1.0 < D_{p,aero} < 10 \mu\text{m}$. Mean values are indicated by the straight line.

diameter particles and/or fewer large diameter particles.

The Ångström exponent for the supermicron aerosol, \hat{a}_{sup} , generally was less than 1 ranging from -1.0 to 0.34 and averaging $-0.52 \pm 17\%$ (Figure 8). In general, the most positive values of \hat{a}_{sup} corresponded to the lowest values of coarse mode surface area and vice versa. An exception to this occurred on DOY 330 and 331, where \hat{a}_{sup} and S_{cs} were elevated above average. $D_{gs,cs}$, however, was shifted to values significantly lower than the mean. Hence both the coarse mode surface area concentration and mean diameter appear to have controlled \hat{a}_{sup} .

The Ångström exponent for the submicron aerosol, \hat{a}_{sub} , was more variable than \hat{a}_{sup} ranging from -0.15 to 2.4 with an average of $1.2 \pm 27\%$. Variability in \hat{a}_{sub} followed changes in S_{acc} such that the highest values of \hat{a}_{sub} were associated with the largest observed values of S_{acc} (DOY 330, 332, 340, 343). An exception to this occurred on day 324 to 325.5 where \hat{a}_{sub} reached a value of 2.4 , while S_{acc} increased only slightly. This high value of \hat{a}_{sub} is uncertain, however, due to very low measured scattering coefficients for this time period.

3.3.3. Single scattering albedo. Single scattering albedo, $\omega_o = \sigma_{sp}/(\sigma_{sp} + \sigma_{ap})$, is a measure of the

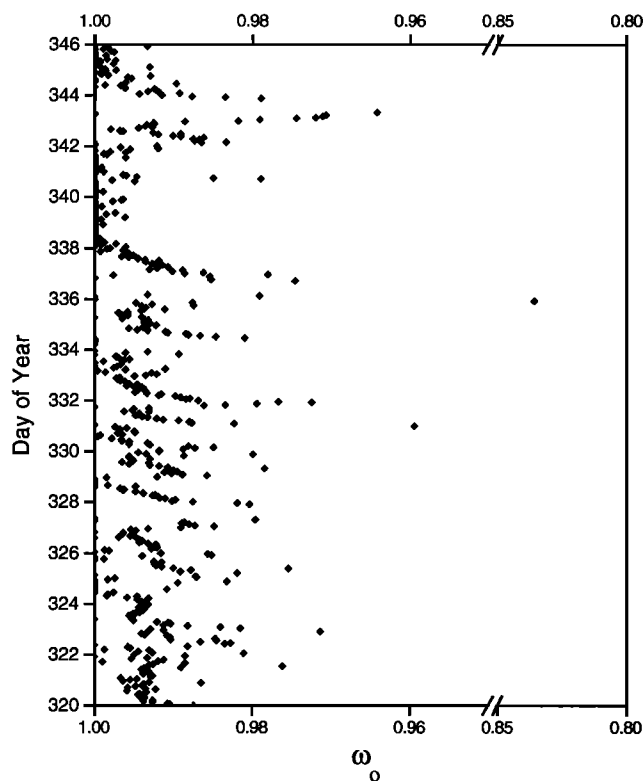


Figure 9. One-hour average values of the single scattering albedo as a function of day of year at a wavelength of 550 nm. Note the axis break at 0.95.

relative magnitude of scattering and absorption by the aerosol. Values for ACE 1 at a wavelength of 550 nm are shown in Figure 9. Laboratory tests have shown that 1.0 to 1.5% of scattering by particles in the sample air is interpreted as absorption by the PSAP (T. Anderson, personal communication, 1997). Values of ω_o presented here have not been corrected for this artifact and therefore are a lower limit. The experiment-average of ω_o was very near one (0.99–0.4%, +1.0%). This is in agreement with the chemical analysis indicating that the majority of both the submicron and supermicron aerosol mass was composed of water soluble ionic species. Values of ω_o decreased to less than 0.97 on only three occasions. Two of these low values were associated with air masses that had passed over Australia prior to reaching the ship (DOY 331.5 and 343). On the basis of calculated trajectories, the third and lowest value, $\omega_o = 0.85$ (DOY 336), corresponded to an air mass with a long MBL residence time. Hence the aerosol was well-aged as evidenced by a relatively large accumulation mode surface mean diameter. Concurrently, low Rn^{222} concentrations indicate the aerosol had not been near land for many days prior to being sampled on the ship. The calculated trajectories indicate the aerosol may have been transported from Madagascar.

3.4. Scattering and Backscattering by the Dominant Aerosol Chemical Components

So far, the discussion of aerosol optical properties has considered only the total aerosol and not the two domi-

nant chemical components, nss SO_4^{2-} and sea salt. Considering the individual components is of importance, however, as determining their relative contribution to total scattering aids in relating aerosol sources to aerosol optical properties.

The calculation of the light scattering by the chemical components was described in section 2.2.2. Figure 10 shows the relative importance of nss SO_4^{2-} and sea-salt aerosol in contributing to total scattering for three air mass types (perturbed marine with high wind speeds; marine with long MBL residence time; and marine with short MBL residence time) at a wavelength of 550 nm. The relatively larger surface area concentration of the nss SO_4^{2-} mode observed in perturbed marine air masses resulted in the highest nss SO_4^{2-} scattering coefficients. The nss SO_4^{2-} aerosol scattering coefficients also were relatively high for marine air masses with long MBL residence times compared to those with short MBL residence times. However, it was sea salt with its high surface area concentration that dominated the total scattering. Throughout ACE 1, the sea-salt mass concentration in the size range 0.2 to 1.0 μm (which is the size range most efficient for scattering) was much larger than the mass concentration of nss SO_4^{2-} . Hence sea salt was the dominant scatterer not only for the supermicron aerosol but also for the submicron aerosol.

Mass concentrations and scattering coefficients for submicron nss SO_4^{2-} and sea salt are shown as a function of day of year in Figure 11. Averages of these values for perturbed marine air masses and for marine air masses with long and short MBL residence times are shown

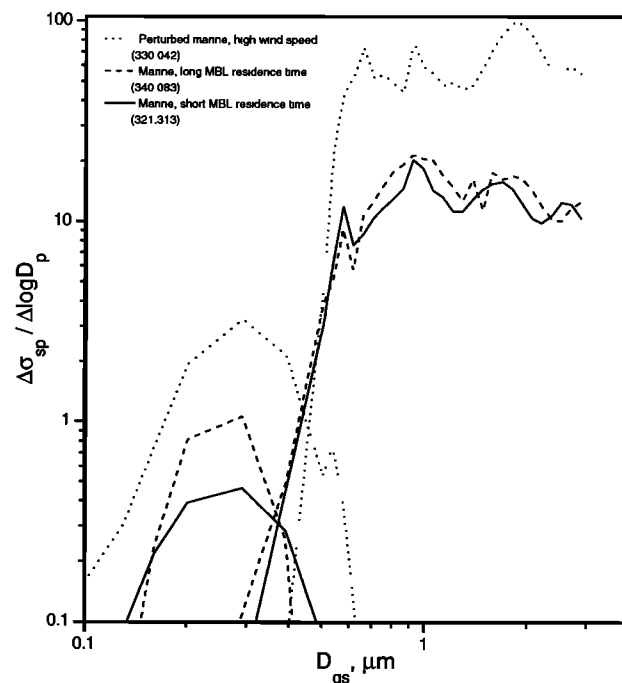


Figure 10. Scattering size distributions calculated from OptiClos for the accumulation (nss SO_4^{2-} aerosol) and coarse (sea-salt aerosol) modes at the instrumental RH (30 to 45%) and 550 nm. Examples are shown for three air mass types.

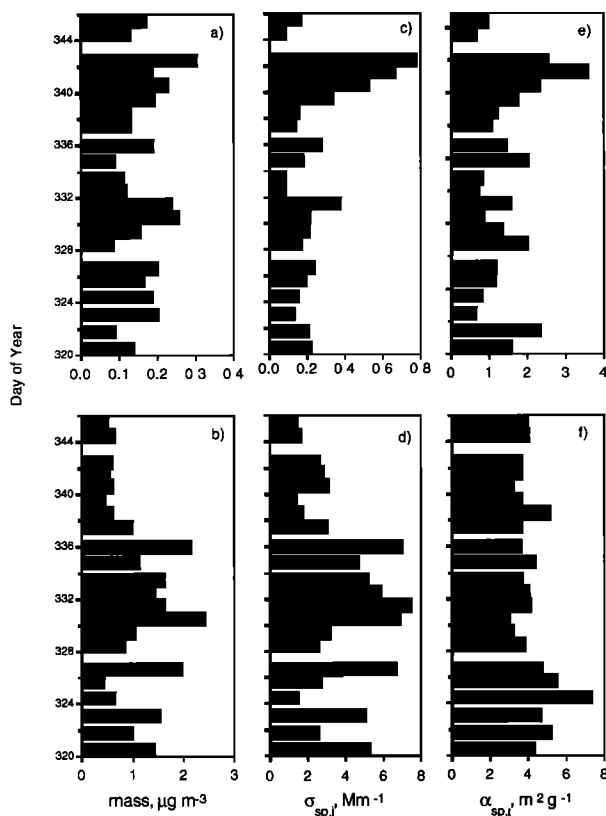


Figure 11. Shown as a function of day of year at instrumental RH (30 to 45%) are mass concentrations of (a) submicron nss sulfate ion as determined by ion chromatography and (b) submicron sea salt; absolute scattering coefficients for (c) submicron nss sulfate aerosol (includes nss SO_4^{2-} , NH_4^+ , and H_2O) and (d) submicron sea salt; and mass scattering efficiencies for (e) submicron nss sulfate ion and (f) submicron sea salt.

in Table 2. On average, nss SO_4^{2-} and sea-salt aerosol made up 20 and 80% of the submicron mass, respectively. Eight percent of the submicron scattering was due to nss SO_4^{2-} , while 92% was due to sea salt. In terms of the total aerosol, $2 \pm 2\%$ of the mass was submicron nss SO_4^{2-} aerosol, $10 \pm 2\%$ was submicron sea salt, and $87 \pm 3\%$ was supermicron sea salt, while $2.5 \pm 2\%$ of the scattering was due to submicron nss SO_4^{2-} , $30 \pm 4\%$ was due to submicron sea salt, and $68 \pm 4\%$ was due to supermicron sea salt. Even though supermicron sea salt dominated the mass concentration of the aerosol, it resulted in only about 70% of the scattering since its size was larger than the size range most efficient for scattering. For the majority of the experiment, the supermicron nss SO_4^{2-} aerosol mass concentration was near the detection limit of $0.3 \mu\text{g m}^{-3}$. Occasionally it, at most, made up 2% of the mass of the total aerosol. As a result, its contribution to scattering was negligible.

Average values of the backscattering coefficients for nss SO_4^{2-} and submicron sea salt aerosol as a function of air mass type also are shown in Table 2. Twenty percent of the submicron backscattering was due to nss SO_4^{2-} aerosol. For the total aerosol, $5 \pm 4\%$ of the backscattering was due to submicron nss SO_4^{2-} , $19 \pm 3\%$ was due

to submicron sea salt, and $75 \pm 4\%$ was due to supermicron sea salt. Hence nss SO_4^{2-} aerosol made a larger contribution to the backscattering than to the scattering by the total aerosol. This is a result of the size dependence of σ_{bsp} versus σ_{sp} as discussed below.

The experiment-average backscattered fraction for submicron nss SO_4^{2-} aerosol was 0.3 ± 0.07 , while that for submicron sea salt was 0.09 ± 0.01 . This difference can be explained by considering the different size ranges of the two components and the size dependence of the backscattered fraction (Figure 12). A submicron value of b for nss SO_4^{2-} aerosol is an integral over diameters from 20 to 800 nm. At the lower end of this size range, b approaches values of 0.5 thereby weighting the integral to a value of 0.3. Alternatively, a submicron value of b for sea salt aerosol is integrated over diameters from about 100 to 1000 nm where b is weighted toward lower values.

The backscattered fraction for the submicron portion of the total aerosol, b_{sub} , averaged 0.11 ± 0.02 . This is closer to b for submicron sea salt (0.09) than for nss SO_4^{2-} aerosol (0.3) indicating that the larger mass concentrations and hence backscattering and scattering coefficients for submicron sea salt in the 0.5 to 1.0 μm size range weighted the submicron backscattered fraction toward the lower value of 0.11.

3.5. Mass Scattering Efficiencies of the Dominant Aerosol Chemical Components

The mass scattering efficiency of an aerosol chemical component j , $\alpha_{\text{sp},j}$, is defined as the change in the scattering by the aerosol ($\partial\sigma_{\text{sp}}$) resulting from a change in the mass of component j (∂m_j) and is given by

$$\alpha_{\text{sp},j} = \frac{\partial\sigma_{\text{sp}}}{\partial m_j} \quad (4)$$

Because it is not possible to measure the derivative of light scattering with respect to component mass, a computational approach was adopted to estimate the component mass scattering efficiencies. Using this method, $\alpha_{\text{sp},j}$ is defined as

$$\alpha_{\text{sp},j} = \frac{\sigma_{\text{sp},j}}{m_j} \quad (5)$$

where $\sigma_{\text{sp},j}$, the scattering coefficient for component j , is estimated as described in section 2.2.2. Mass backscattering efficiencies were calculated by inserting values of $\sigma_{\text{bsp},j}$ into (5). Values of $\alpha_{\text{sp},j}$ and $\alpha_{\text{bsp},j}$ are based on the assumption of an externally mixed aerosol composed of nss sulfate and sea-salt aerosol.

Mass scattering efficiencies were estimated for the submicron fraction of sea-salt aerosol, nss SO_4^{2-} aerosol (including the mass of nss SO_4^{2-} , NH_4^+ , and H_2O), and nss SO_4^{2-} ion. The mass scattering efficiency of submicron nss SO_4^{2-} aerosol was estimated from

$$\alpha_{\text{sp,sub_SO4_aer}} = \frac{\sigma_{\text{sp,sub_SO4_aer}}}{m_{\text{sub_SO4_aer}}} \quad (6)$$

Table 2. Summary of Aerosol Properties for Three Air Mass Types Encountered During ACE 1: Marine, Short MBL Residence Time; Marine, Long MBL Residence Time; and Perturbed Marine

Parameter	Marine, Short MBL ^a Residence Time	Marine, Long MBL ^b Residence Time	Perturbed Marine ^c
$m_{\text{sub_SO4_aer}}$, ^d $\mu\text{g m}^{-3}$	0.15 ± 0.04	0.23 ± 0.02	0.24 ± 0.07
$m_{\text{sub_SO4_ion}}$, ^e $\mu\text{g m}^{-3}$	0.13 ± 0.03	0.21 ± 0.02	0.21 ± 0.06
$m_{\text{sub_sea_salt}}$, ^f $\mu\text{g m}^{-3}$	0.95 ± 0.37	0.87 ± 0.6	1.6 ± 0.73
$m_{\text{sub_aerosol}}$, ^g $\mu\text{g m}^{-3}$	1.1 ± 0.36	1.1 ± 0.57	1.8 ± 0.71
$\sigma_{\text{sp,sub_SO4_aer}}$, Mm^{-1}	0.16 ± 0.05	0.33 ± 0.2	0.38 ± 0.25
$\sigma_{\text{sp,sub_sea_salt}}$, Mm^{-1}	3.2 ± 1.5	3.2 ± 1.8	5.5 ± 2.0
$\sigma_{\text{sp,sub_aerosol}}$, Mm^{-1}	3.4 ± 1.5	3.5 ± 1.7	5.9 ± 1.9
$\sigma_{\text{bsp,sub_SO4_aer}}$, Mm^{-1}	0.05 ± 0.01	0.1 ± 0.04	0.09 ± 0.05
$\sigma_{\text{bsp,sub_sea_salt}}$, Mm^{-1}	0.29 ± 0.13	0.28 ± 0.17	0.5 ± 0.019
$\sigma_{\text{bsp,sub_aerosol}}$, Mm^{-1}	0.34 ± 0.12	0.38 ± 0.14	0.59 ± 0.15
$\alpha_{\text{sp,sub_SO4_aer}}$, $\text{m}^2 \text{g}^{-1}$	0.77 ± 0.26	0.82 ± 0.2	0.94 ± 0.32
$\alpha_{\text{sp,sub_SO4_ion}}$, $\text{m}^2 \text{g}^{-1}$	1.3 ± 0.55	1.6 ± 0.84	1.7 ± 1.0
$\alpha_{\text{sp,sub_sea_salt}}$, $\text{m}^2 \text{g}^{-1}$	4.5 ± 1.1	3.9 ± 0.75	3.8 ± 0.54
$\alpha_{\text{sp,sub_aerosol}}$, $\text{m}^2 \text{g}^{-1}$	3.4 ± 0.58	2.9 ± 0.95	3.2 ± 0.61
$\alpha_{\text{bsp,sub_SO4_aer}}$, $\text{m}^2 \text{g}^{-1}$	0.22 ± 0.06	0.27 ± 0.07	0.22 ± 0.06
$\alpha_{\text{bsp,sub_SO4_ion}}$, $\text{m}^2 \text{g}^{-1}$	0.41 ± 0.14	0.48 ± 0.19	0.40 ± 0.22
$\alpha_{\text{bsp,sub_sea_salt}}$, $\text{m}^2 \text{g}^{-1}$	0.42 ± 0.11	0.33 ± 0.07	0.34 ± 0.06
$\alpha_{\text{bsp,sub_aerosol}}$, $\text{m}^2 \text{g}^{-1}$	0.36 ± 0.06	0.32 ± 0.06	0.32 ± 0.05
$b_{\text{sub_SO4_aer}}$	0.31 ± 0.04	0.35 ± 0.13	0.24 ± 0.04
$b_{\text{sub_sea_salt}}$	0.09 ± 0.007	0.09 ± 0.01	0.09 ± 0.005
$b_{\text{sub_aerosol}}$	0.11 ± 0.01	0.11 ± 0.02	0.10 ± 0.01
$D_{\text{gs,acc}}$, μm	0.18 ± 0.02	0.22 ± 0.05	0.22 ± 0.03
S_{acc} , $\mu\text{m}^2 \text{cm}^{-3}$	4.9 ± 1.7	9.1 ± 3.0	8.3 ± 3.7
$\sigma_{\text{sg,acc}}$	1.5 ± 0.11	1.4 ± 0.11	1.5 ± 0.10

Here the MBL residence time of an air parcel and aerosol it contains is defined as the length of time the parcel spent below 500 mbar prior to being sampled on the ship. Short MBL Residence Time <5 days, Long MBL Residence Time ≥ 5 days. Values are reported for the instrumental RH of 30 to 45% at 550 nm.

^aNumber of samples $n = 12$.

^bValue of $n = 3$.

^cValue of $n = 7$.

^dParameter sub_SO4_aer is submicron sulfate aerosol which includes SO_4^{2-} and associated NH_4^+ mass as determined by ion chromatography (water mass not included).

^eParameter sub_SO4_ion is submicron non-sea-salt (nss) sulfate ion concentration as determined by ion chromatography.

^fParameter sub_sea_salt is submicron Na^+ , K^+ , Mg^{+2} , Ca^{+2} , Cl^- , and sea-salt SO_4^{2-} as determined by ion chromatography.

^gParameter sub_aerosol is sum of submicron sulfate and sea-salt aerosol components.

where $m_{\text{sub_SO4_aer}}$ includes the mass of nss SO_4^{2-} ion, NH_4^+ , and H_2O . The mass scattering efficiency of nss SO_4^{2-} ion was estimated from

$$\alpha_{\text{sp,sub_SO4_ion}} = \frac{\sigma_{\text{sp,sub_SO4_aer}}}{m_{\text{sub_SO4_ion}}} \quad (7)$$

where $m_{\text{sub_SO4_ion}}$ includes only the mass of the nss SO_4^{2-} ion. The latter is a useful quantity as chemical transport models predict the ion concentration or column burden of sulfate rather than the sulfate aerosol ($\text{SO}_4^{2-} + \text{NH}_4^+ + \text{H}_2\text{O}$) concentration [e.g., Langner and Rodhe, 1991]. Finally, the mass scattering efficiency of the total submicron aerosol was estimated.

Average values of the mass scattering and backscattering efficiencies of the submicron chemical compo-

nents and total aerosol are listed for different air mass types in Table 2 and are shown as a function of day of year in Figure 11. Values of $\alpha_{\text{sp,sub_SO4_ion}}$ estimated at the instrumental RH (30 to 45%) ranged from 0.7 to $3.6 \text{ m}^2 \text{g}^{-1}$. Values for marine air masses with short MBL residence times were, on average, the lowest at $1.3 \pm 0.55 \text{ m}^2 \text{g}^{-1}$. This compares to an average of $1.7 \pm 1.0 \text{ m}^2 \text{g}^{-1}$ for perturbed marine air masses and $1.6 \pm 0.84 \text{ m}^2 \text{g}^{-1}$ for marine air masses with long MBL residence times. Overall, however, values of $\alpha_{\text{sp,sub_SO4_ion}}$ did not vary greatly between different air mass types indicating the relative stability in the mean diameter (experiment-wide-relative standard deviation (r.s.d.) equal to $\pm 16\%$) and geometric standard deviation (r.s.d. equal to $\pm 7\%$) of the sulfate mode.

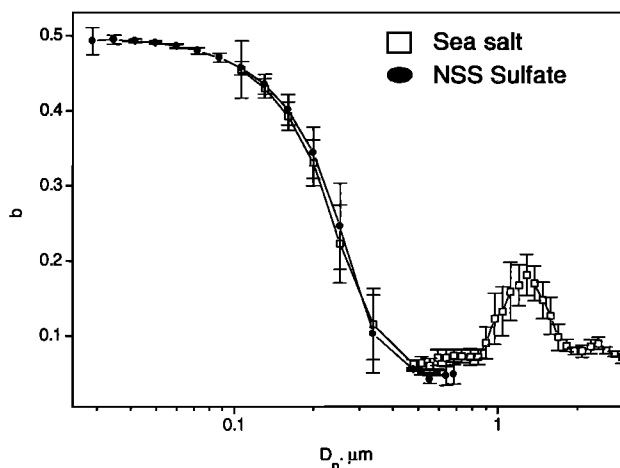


Figure 12. Size distribution of the backscattered fraction, b , for the nss SO_4^{2-} and sea-salt components. The size distribution of the nss SO_4^{2-} and sea-salt components is based on the lognormal fitting of the measured size distribution.

Mass scattering efficiencies for submicron sea salt, $\alpha_{\text{sp,sub-sea-salt}}$ ranged from 3 to $7.3 \text{ m}^2 \text{ g}^{-1}$. These larger values relative to $\alpha_{\text{sp,sub-SO}_4\text{-ion}}$ result from the tailing of coarse mode sea salt into the mid to upper end of the accumulation mode size range or into the size range which is most efficient for light scattering. Given the similar lifetimes of submicron nss SO_4^{2-} and sea-salt aerosol and the large values of $\alpha_{\text{sp,sub-sea-salt}}$, the importance of submicron sea salt in controlling the scattering by MBL aerosol in this remote Southern Ocean region is evident.

Mass backscattering efficiencies also were calculated for submicron nss SO_4^{2-} and submicron sea-salt aerosol (Table 2). Values for the two components are similar as a result of the size range of the two components and the size dependence of the backscattering coefficient.

The values estimated here for $\alpha_{\text{sp,sub-SO}_4\text{-ion}}$ are lower than those previously reported for Pacific Ocean aerosol. Quinn *et al.* [1996] estimated average values of 5.1 ± 0.21 and $3.8 \pm 0.35 \text{ m}^2 \text{ g}^{-1}$ for two cruises carried out in the central Pacific. The lower overall average of $\alpha_{\text{sp,sub-SO}_4\text{-ion}}$ for the ACE 1 region corresponds to lower values of $D_{\text{gs,acc}}$ relative to those observed in different regions of the Pacific. $D_{\text{gs,acc}}$ averaged $0.20 \pm 0.04 \text{ } \mu\text{m}$ during ACE 1, while Pacific Ocean values ranged from 0.21 to $0.26 \text{ } \mu\text{m}$. The lower average value for ACE 1 may be a result of an average shorter MBL residence time. Values of $\alpha_{\text{sp,sub-sea-salt}}$ for the ACE 1 region were similar to those previously reported for the Pacific Ocean.

4. Conclusions

The measurements reported here from ACE 1 have allowed for the characterization of the optical properties of the marine boundary layer aerosol in terms of its chemical and physical properties in the Southern Ocean

region. The anthropogenic influence on the aerosol in this remote marine region is minimal. As a result, the average concentration of nss SO_4^{2-} aerosol during ACE 1 was lower than that observed for the central Pacific Ocean by a factor of 3 [Quinn *et al.*, 1996]. The low nss SO_4^{2-} concentrations coupled with appreciable sea salt concentrations (comparable, on average, to those reported for the Pacific Ocean [Quinn *et al.*, 1996]) result in sea salt being the dominant chemical component controlling aerosol optical properties.

The majority of the scattering by both submicron and supermicron aerosol was due to sea salt. The hemispheric backscattered fraction for the submicron aerosol averaged 0.11 ± 0.02 and was controlled by the tailing of coarse mode sea salt into the submicron size range. The backscattered fraction for the supermicron aerosol, which also was controlled by sea-salt mass concentrations, averaged 0.13 ± 0.01 .

Concentrations of nss SO_4^{2-} aerosol were largest in air masses that had been transported over Australia and in marine air masses with MBL residence times of at least 5 days. The larger sulfate concentrations coupled with larger accumulation mode surface mean diameters resulted in these same air masses having the highest calculated mass scattering efficiencies for submicron nss SO_4^{2-} . Mass scattering efficiencies for submicron sea salt were higher, however, due to the tailing of coarse mode sea salt into the particle size range most efficient for light scattering. Calculated mass backscattering efficiencies were comparable for the two components due to increased backscattering in the size range corresponding to that of the nss SO_4^{2-} mode.

Acknowledgments. We thank M. Hamilton, D. Hamilton, and J. Johnson for analytical and logistical assistance, the officers and crew of the *Discoverer* for their cooperation, and T. Anderson for instructive comments. This research was funded by the Aerosol Component of the NOAA Climate and Global Change Program. This research is a contribution to the International Global Atmospheric Chemistry (IGAC) Core project of the International Geosphere-Biosphere Programme (IGBP) and is part of the IGAC Aerosol Characterization Experiments (ACE). This is NOAA PMEL contribution 1849 and JISAO contribution 444.

References

- Anderson, T. L., et al., Performance characteristics of a high-sensitivity, three-wavelength, total scatter/backscatter nephelometer, *J. Atmos. Oceanic Technol.*, **13**, 967–986, 1996.
- Ayers, G. P., J. P. Ivey, and R. W. Gillett, Coherence between seasonal cycles of dimethyl sulfide, methanesulfonate, and sulfate in marine air, *Nature*, **349**, 404–406, 1991.
- Bates, T. S., V. N. Kapustin, P. K. Quinn, D. S. Covert, D. J. Coffman, C. Mari, P. A. Durkee, W. DeBruyn, and E. Saltzman, Processes controlling the distribution of aerosol particles in the lower marine boundary layer during ACE 1, *J. Geophys. Res.*, this issue.
- Berg, O. H., E. Swietlicki, and R. Krejci, Hygroscopic growth of aerosol particles in the marine boundary layer

- over the Pacific and Southern oceans during ACE 1, *J. Geophys. Res.*, this issue.
- Berner, A., C. Lurzer, F. Pohl, O. Preining, and P. Wagner, The size distribution of the urban aerosol in Vienna, *Sci. Total Environ.*, **13**, 245–261, 1979.
- Bohren, C. F., and D. R. Huffman, *Absorption and Scattering of Light by Small Particles*, John Wiley, New York, 1983.
- Bray, W. H., Water vapor pressure control with aqueous solutions of sulfuric acid, *J. Mater.*, **5**, 233–248, 1970.
- Bromley, L. A., Thermodynamic properties of strong electrolytes in aqueous solutions, *AIChE J.*, **19**, 313–320, 1973.
- Charlson, R. J., J. Langner, H. Rodhe, C. B. Leovy, and S. G. Warren, Perturbation of the northern hemisphere radiative balance by backscattering from anthropogenic sulfate aerosols, *Tellus, Ser. B*, **43**, 152–163, 1991.
- Clarke, A. D., Atmospheric nuclei in the Pacific midtroposphere: Their nature, concentration, and evolution, *J. Geophys. Res.*, **98**, 20,633–20,647, 1993.
- Draxler, R. R., Hybrid Single-Particle Lagrangian Integrated Trajectories (HY-SPLIT): Version 3.0, User's guide and model description, *Tech. Rep. ERL ARL-195*, Natl. Oceanic and Atmos. Admin., Silver Spring, Md., 1992.
- Gathman, S. G., Optical properties of the marine aerosol as predicted by the Navy aerosol model, *Opt. Eng.*, **22**, 57, 1983.
- Gong, S. L., L. A. Barrie, and J.-P. Blanchet, Modeling sea-salt aerosols in the atmosphere, 1, Model development, *J. Geophys. Res.*, **102**, 3805–3818, 1997.
- Gras, J. L., and G. P. Ayers, Marine aerosol at southern midlatitudes, *J. Geophys. Res.*, **88**, 10,661–10,666, 1983.
- Hainsworth, A. H. W., A. L. Dick, and J. L. Gras, Climatic context of ACE 1: A meteorological and chemical overview, *J. Geophys. Res.*, this issue.
- Heintzenberg, J., The angular calibration of the total scatter/backscatter nephelometer, consequences and applications, *Staub Reinhalt. Luft*, **38**, 62–63, 1978.
- Hoppel, W. A., G. M. Frick, and R. E. Larson, Effect of nonprecipitating clouds on the aerosol size distribution in the marine boundary layer, *Geophys. Res. Lett.*, **13**, 125–128, 1986.
- Hoppel, W. A., G. M. Frick, J. W. Fitzgerald, and R. E. Larson, Marine boundary layer measurements of new particle formation and the effects nonprecipitating clouds have on the aerosol size distribution, *J. Geophys. Res.*, **99**, 14,443–14,459, 1994.
- Langner, J., and H. Rodhe, A global three-dimensional model of the tropospheric sulfur cycle, *J. Atmos. Chem.*, **13**, 225–263, 1991.
- Marshall, S. F., Measurement-derived radiative transfer parameters for the aerosol climate forcing problem, M.S. dissertation, Univ. of Washington, Seattle, 1994.
- McInnes, L. M., P. K. Quinn, D. S. Covert, and T. L. Anderson, Gravimetric analysis, ionic composition, and associated water mass of the marine aerosol, *Atmos. Environ.*, **30**, 869–884, 1996.
- Mestayer, P. G., A. M. J. Van Eijk, G. De Leeuw, and B. Tranchant, Numerical simulation of the dynamics of sea spray over the waves, *J. Geophys. Res.*, **101**, 20,771–20,797, 1996.
- O'Dowd, C. D., and M. H. Smith, Physicochemical properties of aerosols over the Northeast Atlantic: Evidence for wind-speed-related submicron sea-salt aerosol production, *J. Geophys. Res.*, **98**, 1137–1149, 1993.
- O'Dowd, C. D., M. H. Smith, I. E. Consterdine, and J. A. Lowe, Marine aerosol, sea-salt, and the marine sulfur cycle: A short review, *Atmos. Environ.*, **31**, 73–80, 1997.
- Penner, J. E., R. Dickinson, and C. O'Neill, Effects of aerosol from biomass burning on the global radiation budget, *Science*, **256**, 1432–1434, 1992.
- Pilinis, C., and J. H. Seinfeld, Continued development of a general equilibrium model for inorganic multicomponent atmospheric aerosols, *Atmos. Environ.*, **21**, 2453–2466, 1987.
- Pitzer, K. S., and G. Mayorga, Thermodynamics of electrolytes, II, Activity and osmotic coefficients for strong electrolytes with one or both ions univalent, *J. Phys. Chem.*, **77**, 2300–2308, 1973.
- Pszenny, A. A. P., A. J. Castelle, R. A. Duce, and J. N. Galloway, A study of the sulfur cycle in the Antarctic marine boundary layer, *J. Geophys. Res.*, **94**, 9818–9830, 1989.
- Quinn, P. K., and D. J. Coffman, Local closure during ACE 1: Aerosol mass concentration and scattering and backscattering coefficients, *J. Geophys. Res.*, this issue.
- Quinn, P. K., T. S. Bates, J. E. Johnson, D. S. Covert, and R. J. Charlson, Interactions between the sulfur and reduced nitrogen cycles over the central Pacific Ocean, *J. Geophys. Res.*, **95**, 16,405–16,416, 1990.
- Quinn, P. K., W. E. Asher, and R. J. Charlson, Equilibria of the marine multiphase ammonia system, *J. Atmos. Chem.*, **14**, 11–30, 1992.
- Quinn, P. K., D. S. Covert, T. S. Bates, V. N. Kapustin, D. C. Ramsey-Bell, and L. M. McInnes, Dimethylsulfide/cloud condensation nuclei/climate system: Relevant size-resolved measurements of the chemical and physical properties of atmospheric aerosol particles, *J. Geophys. Res.*, **98**, 10,411–10,427, 1993.
- Quinn, P. K., S. F. Marshall, T. S. Bates, D. S. Covert, and V. N. Kapustin, Comparison of measured and calculated aerosol properties relevant to the direct radiative forcing of tropospheric sulfate aerosol on climate, *J. Geophys. Res.*, **100**, 8977–8992, 1995.
- Quinn, P. K., V. N. Kapustin, T. S. Bates, and D. S. Covert, Chemical and optical properties of marine boundary layer aerosol particles of the mid-Pacific in relation to sources and meteorological transport, *J. Geophys. Res.*, **101**, 6931–6951, 1996.
- Robinson, R. A., and R. H. Stokes, *Electrolyte Solutions*, 2nd ed., Butterworths, London, 1965.
- Rood, M. J., M. A. Shaw, T. V. Larson, and D. S. Covert, Ubiquitous nature of ambient metastable aerosol, *Nature*, **337**, 537–539, 1989.
- Savoie, D. L., and J. M. Prospero, Particle size distribution of nitrate and sulfate in the marine atmosphere, *Geophys. Res. Lett.*, **9**, 1207–1210, 1982.
- Smith, M. H., I. E. Consterdine, and P. M. Park, Atmospheric loadings of marine aerosol during a Hebridean cyclone, *Q. J. R. Meteorol. Soc.*, **115**, 383–395, 1989.
- Sokolik, I. N., and O. B. Toon, Direct radiative forcing by anthropogenic mineral aerosols, *Nature*, **381**, 681–683, 1996.
- Stelson, A. W., Urban aerosol refractive index prediction by partial molar refraction approach, *Environ. Sci. Technol.*, **24**, 1676–1679, 1990.
- Tang, I. N., and H. R. Munkelwitz, Simultaneous determination of refractive index and density of an evaporating aqueous solution droplet, *Aerosol. Sci. Technol.*, **15**, 201–207, 1991.
- Tang, I. N., and H. R. Munkelwitz, Water activities, densities, and refractive indices of aqueous sulfates and sodium nitrate droplets of atmospheric importance, *J. Geophys. Res.*, **99**, 18,801–18,808, 1994.
- Whitby, K. T., The physical characteristics of sulfur aerosols, *Atmos. Environ.*, **12**, 135–159, 1978.
- Whittlestone, S., and W. Zahorowski, Baseline radon detectors for shipboard use: Development and deployment in ACE 1, *J. Geophys. Res.*, this issue.

Young, J. F., Humidity control in the laboratory using salt-solutions—A review, *J. Appl. Chem.*, 17, 241–245, 1967.
Zdanovskii, A. B., Tr. Solyanoi Lab. Vses. Inst. Galurgii Akad. Nauk, SSSR, no. 6, 1936.

T. S. Bates, D. J. Coffman, V. N. Kapustin, and P. K. Quinn, Pacific Marine Environmental Laboratory, NOAA, 7600 Sand Point Way NE, Seattle, WA 98115.

(e-mail: bates@pmel.noaa.gov; derek@pmel.noaa.gov; kapustin@soest.hawaii.edu; quinn@pmel.noaa.gov)

D. S. Covert, Department of Atmospheric Sciences, University of Washington, Seattle, WA 98195. (d.covert@u.washington.edu)

(Received May 30, 1997; revised August 7, 1997; accepted August 13, 1997.)